Received: 11 November 2021 | Revised: 17 January 2022 | Accepted: 18 January 2022

DOI: 10.1002/ppap.202100205

RESEARCH ARTICLE

PLASMA PROCESSES AND POLYMERS

# Operation mode recognition of surface microdischarge based on the gray level histogram

**Chen Lu** | **Zilan Xiong**

State Key Laboratory of Advanced Electromagnetic Engineering and Technology, Huazhong University of Science and Technology, Wuhan, Hubei, China

**Correspondence**
Zilan Xiong, State Key Laboratory of Advanced Electromagnetic Engineering and Technology, Huazhong University of Science and Technology, Wuhan, 430074 Hubei, China.
Email: zilanxiong@hust.edu.cn

**Funding information**
National Natural Science Foundation of China, Grant/Award Numbers: 51907076, 52177145

**Abstract**

A visible image of gas discharge contains rich information. This study investigates the visible light information of surface microdischarge (SMD) under different operation modes and develops a method to realize online monitoring of the operation modes based on a gray level histogram (GLH). Two SMD sources were used to verify the effectiveness of the method. The distribution curve in the GLH gradually shifted to a large gray level as the operation mode transferred from ozone mode to $NO_x$ mode. The mean, variance, energy, entropy, and uniformity threshold values used to distinguish the operation modes were found to be approximately the same in both sources. Finally, a simplified distribution map based only on entropy and uniformity is proposed for the fast operation mode recognition of SMD.

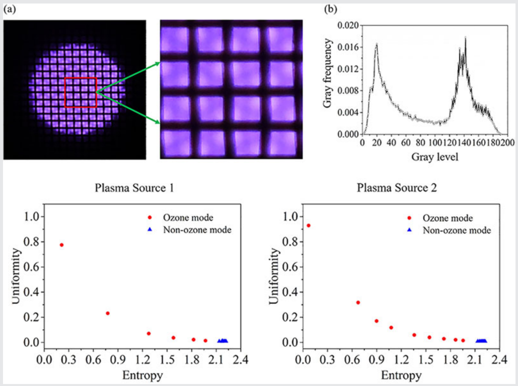

**KEYWORDS**

GLH features, gray level histogram (GLH), operation mode transformation recognition, surface microdischarge (SMD), visible image

## 1 | INTRODUCTION

Cold atmospheric pressure plasmas (CAPs) have been widely researched and developed in recent years.[1–3] Compared to low-pressure plasmas, CAPs do not require complicated vacuum systems, and their gas temperature is close to room temperature.[4,5] Surface microdischarge (SMD) belongs to the class of CAPs,[6] and it usually consists of a powered electrode, a dielectric sheet, and a mesh electrode with a sandwich structure. SMD is a variation of dielectric barrier discharge (DBD), its processing area is large, and the discharge is uniform and stable.[7,8] Compared with other CAP sources, the SMD structure is simple and does not require special rare gases.[9,10] Because SMD has the advantages of a simple discharge form, rich chemical reaction, and diverse products, it has been applied in many fields, such as biomedicine,[11,12] material processing,[13,14] agriculture,[15,16] aerotechnics,[17,18] food preservation,[19,20] and environmental protection.[21,22]

There are three different operation modes for SMD based on the dominant gas phase products, namely, the ozone, transition, and $NO_x$ modes.[23–27] In the ozone mode, the main gas phase production of SMD is $O_3$; in the transition mode, the main gas phase production is $O_3$ and $NO_x$, and $O_3$ gradually disappear after some time; in the $NO_x$ mode, the main gas phase production is NO, $NO_2$, HONO, and $HNO_3$.[28] Different SMD operation modes are aimed at different applications. Pavlovich et al.[23] studied the influence of different SMD operation modes on the bacterial inactivation effect and found that sterilization relied significantly on the operation mode ($NO_x$ mode > transition mode > ozone mode). Lu et al.[29] used an SMD device to modify the mechanical properties of decellularized porcine aortic valve leaflets (DPAVL). The results indicated that the mechanical properties of DPAVL could be significantly improved when the SMD device worked in the $NO_x$ mode rather than the ozone mode. Capelli et al.[30] used an SMD device in ozone mode for food packaging decontamination from SARS-Cov-2 RNA and found that the viral RNA can be completely eliminated after 10 min of plasma treatment without affecting the performance of packaging materials and the shelf-life of packaged products. The SMD in different operation modes has different effects on processed objects.[31–33]

The current main methods used to determine the operation modes of SMD usually use spectrometers, ozone detectors, or $NO_x$ detectors by directly detecting the gas phase products under different operation modes.[34–36] These methods are valid; however, they have the disadvantages of high cost, complicated operation, and are time-consuming. Developing fast-responding, reliable, and low-cost diagnostic methods for the SMD operation mode recognition is important for its industrial application.

The continuous development of digital image processing technology has recently enabled its introduction in the field of CAP diagnostics. Wu et al.[37] identified the homogeneous and filamentary discharge of DBD by analyzing the gray level histogram (GLH) of the DBD discharge image and verified the effectiveness of the method by changing the applied voltage ($V_{p–p}$), power frequency, and exposure time. Guo et al.[38] divided the alternating current (AC) corona discharge stages and analyzed the AC corona discharge spatial structure by capturing color images of the AC corona discharge and using RGB and HSI chromaticity indicators. Zou et al.[39] quantified the long-lived species ($H_2O_2$ and $NO_2^-$) in plasma-activated water produced by pin-plate discharge or SMD using a digital colorimetry-based method. Prasad et al.[40] used a color thresholding-based image segmentation method to extract the effective spread of corona plasma and analyzed the correlation between the image parameters and the corona power. CAP diagnostics based on digital image processing technology is a simple to use, low cost, and high real-time performance noninvasive diagnostic method, which is expected to become an efficient online diagnostic method.

The limited literature mainly focuses on using digital images to determine the characteristics of the discharge, such as discharge type and homogeneity. The correlation between the visible image and gas phase products has rarely been mentioned. Our previous study analyzed the relationship between the RGB components extracted from the discharging image and the power consumption and mode transformation. It was found that the curve of (B–G)% and the $V_{p–p}$ could be used to distinguish between the ozone and non-ozone modes.[41] However, this method still required a $V_{p–p}$ to obtain precise mode recognition.

This study further investigates the relationship between the GLH features of the visible image of SMD and mode transformation. Fourier transform infrared spectrometry (FTIR) was used to identify the SMD gas phase products under different voltages to determine the operation mode at different voltages for two different plasma sources. A digital camera was used to capture the discharge images of the SMD in the corresponding operation modes. The GLH of the discharge images was obtained using digital image processing technology. An SMD operation mode recognition method based on the related feature distribution characteristics of GLH is proposed for the first time in this paper.

## 2 | EXPERIMENTAL SETUP AND MEASUREMENTS

### 2.1 | Experimental setup

Figure 1 shows the structure of the SMD device used in this study. The teflon-wrapped copper electrode was 20 mm in diameter and 14 mm in height. A 50-mm-diameter stainless-steel mesh with a cell density of 5 × 5 cells/$cm^2$ was used as the ground electrode. A 50-mm-diameter $Al_2O_3$ dielectric sheet was attached between power and ground electrodes. The SMD device was placed over a 38-mm diameter and 45-mm-high cylindrical acrylic chamber. Two 13-mm-diameter ZnSe windows were mounted on the wall of the cylindrical acrylic chamber to transmit the infrared (IR) beam to analyze the composition of the gas phase products generated by the SMD device. The FTIR path length is

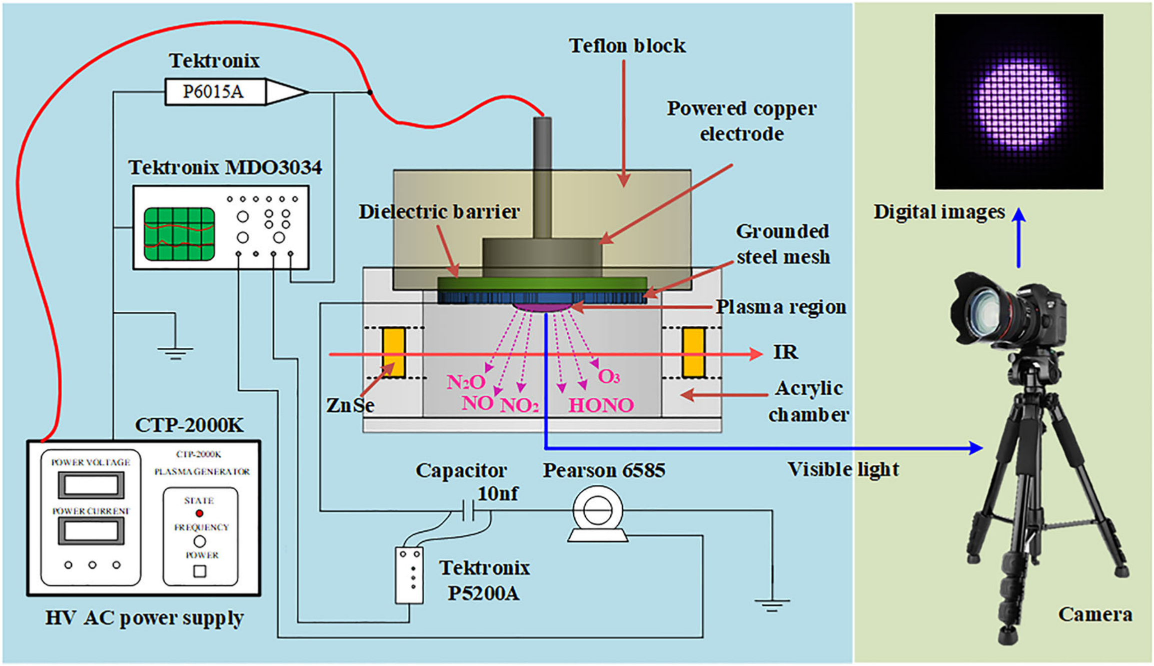

FIGURE 1 Schematic diagram of the surface microdischarge device and the experimental setup

50 mm. A high-voltage and high-frequency AC power supply (CTP-2000K; Corona Lab) was used as the power source.

To explore the visible light information in different operation modes and test the feasibility of the proposed method based on visible images, two SMD sources were introduced by changing the thickness of the dielectric sheet. SMDs with 0.5- and 1-mm-thick dielectric sheets were named as plasma source 1 and plasma source 2, respectively.

## 2.2 | Measurements and methods

The waveform frequency for all experiments was fixed at 8 kHz. The applied AC voltage amplitude was monitored using a voltage probe (Tektronix P6015A) and an oscilloscope (Tektronix MDO3034). The circuit current was measured using a current probe (Pearson 6585). A 10 nf capacitor was connected in series between the mesh and ground. The voltage across the capacitor was measured using a differential probe (Tektronix P5200A). The power consumed by the SMD device was obtained according to the Lissajous method.

FTIR (VERTEX 70; Bruker) was used as an in situ diagnostic of the chemical composition of the gas phase products generated by the SMD. The wavenumber resolution of the FTIR measurements was set to 4 $cm^{-1}$, and 16 scans were averaged to create each spectrum. The time resolution of each spectrum was 15 s. The primary gas phase products generated by the SMD device included $N_2O$, NO, $NO_2$, HONO, and $O_3$.

A digital camera (NIKON D750) was used to obtain the discharge images of the SMD at different $V_{p-p}$ against a dark background. The main camera parameters were set as follows: aperture (f) of 5.6, exposure time ($T$) of 1 s, and ISO of 2000. The remaining parameters were set as the default values. To avoid noise interference from the surrounding environment, the denoising and filtering measurements on the captured discharge images were performed as follows: (a) five SMD discharge images were captured continuously at the same voltage, while other conditions remained unchanged; (b) the image, when the $V_{p-p}$ was 0 kV, was set as the background image. The discharge images of the SMD were compared with the background image to eliminate the background noise interference; (c) for the same voltage, the final results were the average of five consecutive images.

To further eliminate the interference of noise, partial areas of the discharge images of the SMD were selected for analysis, as shown in Figure 2a. The real dimension of the selected area of the discharge images was $6.3 \times 6.3$ mm. The color image of the discharge was converted into a grayscale image, and the frequency of occurrence of each gray level was counted. The horizontal axis of the GLH represents each gray level appearing in the grayscale image and its value ranged from 0 to 255, whereas the vertical axis represents the frequency of each gray level and its value ranged from 0 to 1. Figure 2b shows the GLH corresponding to Figure 2a.

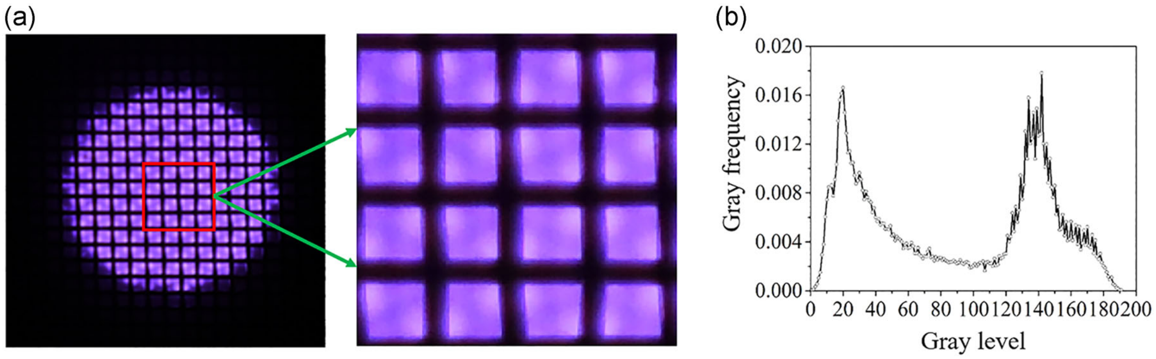

**FIGURE 2** (a) Analysis area of the discharge images. The $Al_2O_3$ dielectric sheet was 0.5-mm-thick and the $V_{p-p}$ was 6 kV. (b) Gray level histogram corresponding to (a)

The frequency reached a maximum value of 0.018 at a gray level of 142.

The GLH was quantitatively analyzed by extracting the mean, variance, energy, entropy, and uniformity values from the GLH. The mean is a measure of the average gray level of the discharge image. The larger the average value, the brighter the discharge image, and the smaller the average value responses for a darker discharge image. The calculation for the mean of the gray levels is shown in Equation (1). Variance is a measure of the dispersion of the gray level of the discharge image relative to the average gray level. The greater the variance, the more scattered the gray level of the discharge image relative to the mean, and vice versa. The calculation for the gray level variance is shown in Equation (2). Energy is a measure of the thickness of the texture of a discharge image. Greater energy indicates that the grayscale image is in a more uniform and regularly changing texture mode. The calculation for the energy of the gray levels is shown in Equation (3). Entropy is a measure of the amount of information contained in a discharge image. The greater the entropy, the more information the image contains. The calculation for the entropy of the gray levels is given by Equation (4). Uniformity is a measure of the consistency of a discharge image. The uniformity is highest when all gray levels in the discharge images are the same. The calculation for the uniformity of the gray levels is shown in Equation (5).

$$\boldsymbol{R}_{\text{mean}} = \sum_{i=0}^{L} \boldsymbol{Z_i P(Z_i)}, \tag{1}$$

$$\boldsymbol{R}_{\text{variance}} = \sum_{i=0}^{L} [\boldsymbol{Z_i} - \boldsymbol{R_{mean}}]^2 \boldsymbol{P(Z_i)}, \tag{2}$$

$$\boldsymbol{R}_{\text{energy}} = \sum_{i=0}^{L} \boldsymbol{Z_i}^2 \boldsymbol{P(Z_i)}, \tag{3}$$

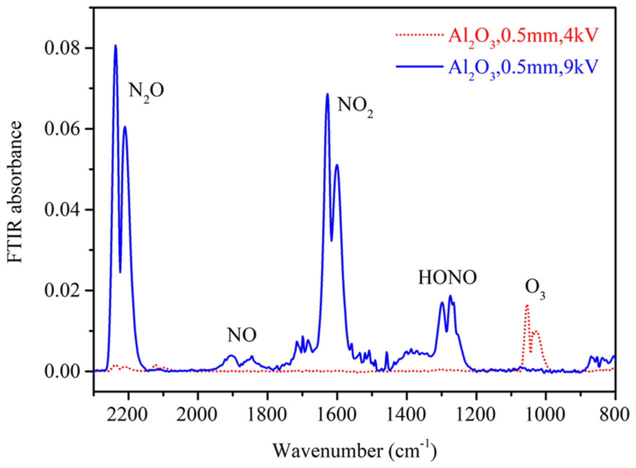

**FIGURE 3** Typical Fourier transform infrared spectrometry (FTIR) spectra of the surface microdischarge device under different $V_{p-p}$

$$\boldsymbol{R}_{\text{entropy}} = -\sum_{i=0}^{L} \boldsymbol{P(Z_i)\log_2 P(Z_i)}, \tag{4}$$

$$\boldsymbol{R}_{\text{uniformity}} = \sum_{i=0}^{L} \boldsymbol{P(Z_i)}^2, \tag{5}$$

where $Z_i$ is the gray level, $P(Z_i)$ is the frequency corresponding to $Z_i$, and $L$ is the total number of gray levels.

## 3 | RESULTS

### 3.1 | Division of the operation modes for SMD using FTIR

Figure 3 shows the typical FTIR spectra of the SMD device (plasma source 1). The main gas product at a $V_{p-p}$ of 4 kV was $O_3$ (1055 cm$^{-1}$); therefore, the SMD device was defined as operating in ozone mode. When the $V_{p-p}$

increased to 9 kV, the main gas phase product of the SMD was nitrogen oxides, including NO at 1900 cm$^{-1}$, $NO_2$ at 1630 cm$^{-1}$, and HONO at 1255 cm$^{-1}$, and the SMD was defined as operating in the $NO_x$ mode.

As $O_3$ will eventually disappear in the transition mode and with the final gas phase products being the same as in the $NO_x$ mode,[42] the operation mode in this study was simply defined as the ozone and non-ozone modes (including the transition mode and $NO_x$ mode).

Figure 4 shows the distinct operation modes, as determined by FTIR, of the two different plasma sources at different $V_{p\text{–}p}$. When the $V_{p\text{–}p}$ value of plasma source 1 was 2.5–5 kV, the SMD operated in the ozone mode. When the $V_{p\text{–}p}$ value exceeded 5.5 kV, the SMD operated in the non-ozone mode. When the $V_{p\text{–}p}$ value of plasma source 2 was 3–7 kV, the SMD operated in the ozone mode. When the $V_{p\text{–}p}$ value exceeded 7.5 kV, the SMD operated in the non-ozone mode.

## 3.2 | Typical discharging visible color images of SMD

Figure 5 shows the discharging visible color images of the two different plasma sources at different $V_{p\text{–}p}$. As the $V_{p\text{–}p}$ for the same plasma source increased, the discharge power consumption of the SMD device increased, the discharge intensity became more severe, the discharge brightness became stronger, and the discharge area became larger. When the $V_{p\text{–}p}$ remained constant, the discharge power consumption of plasma source 1 was greater than that of plasma source 2,[42] and the discharge intensity, discharge brightness, and discharge area were larger than those of plasma source 2.

## 3.3 | GLH of the SMD under different $V_{p\text{–}p}$

Figure 6 shows the GLH of the two different plasma sources at different $V_{p\text{–}p}$. The gray frequency at a 0–10 gray level was an order higher than that at a 10–255 gray level. In the 0–10 gray level range, the gray frequency decreased with an increase in the $V_{p\text{–}p}$. As the $V_{p\text{–}p}$ was increased, the gray frequency distribution curve in the 10–255 gray level range gradually exhibited two peaks, and the interval between the two peaks increased and shifted to the right. The peak value of the first peaks decreased with an increase in the $V_{p\text{–}p}$, while the peak value of the second peak increased.

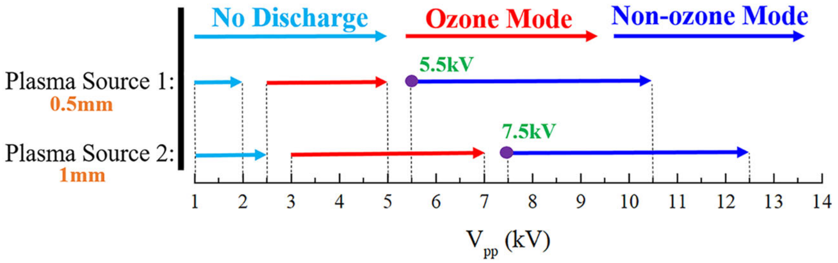

**FIGURE 4** Division of the operation modes for the two different plasma sources as determined by Fourier transform infrared spectrometry

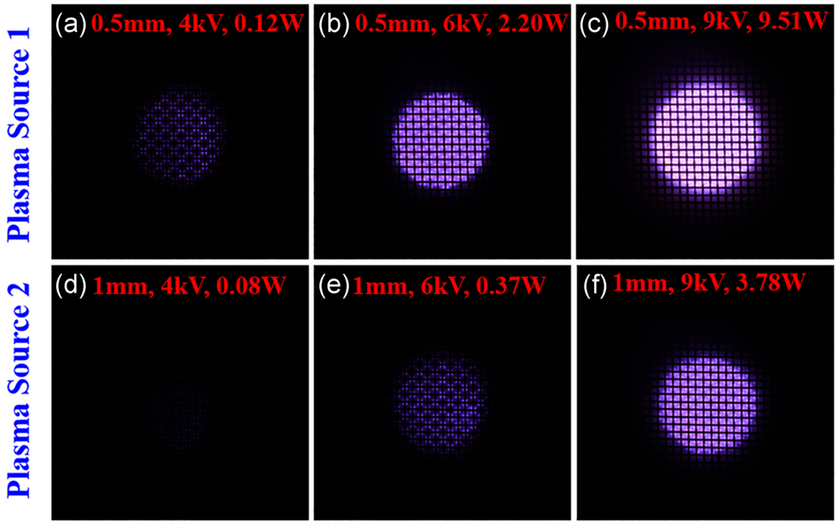

**FIGURE 5** Discharging color images for the two different plasma sources

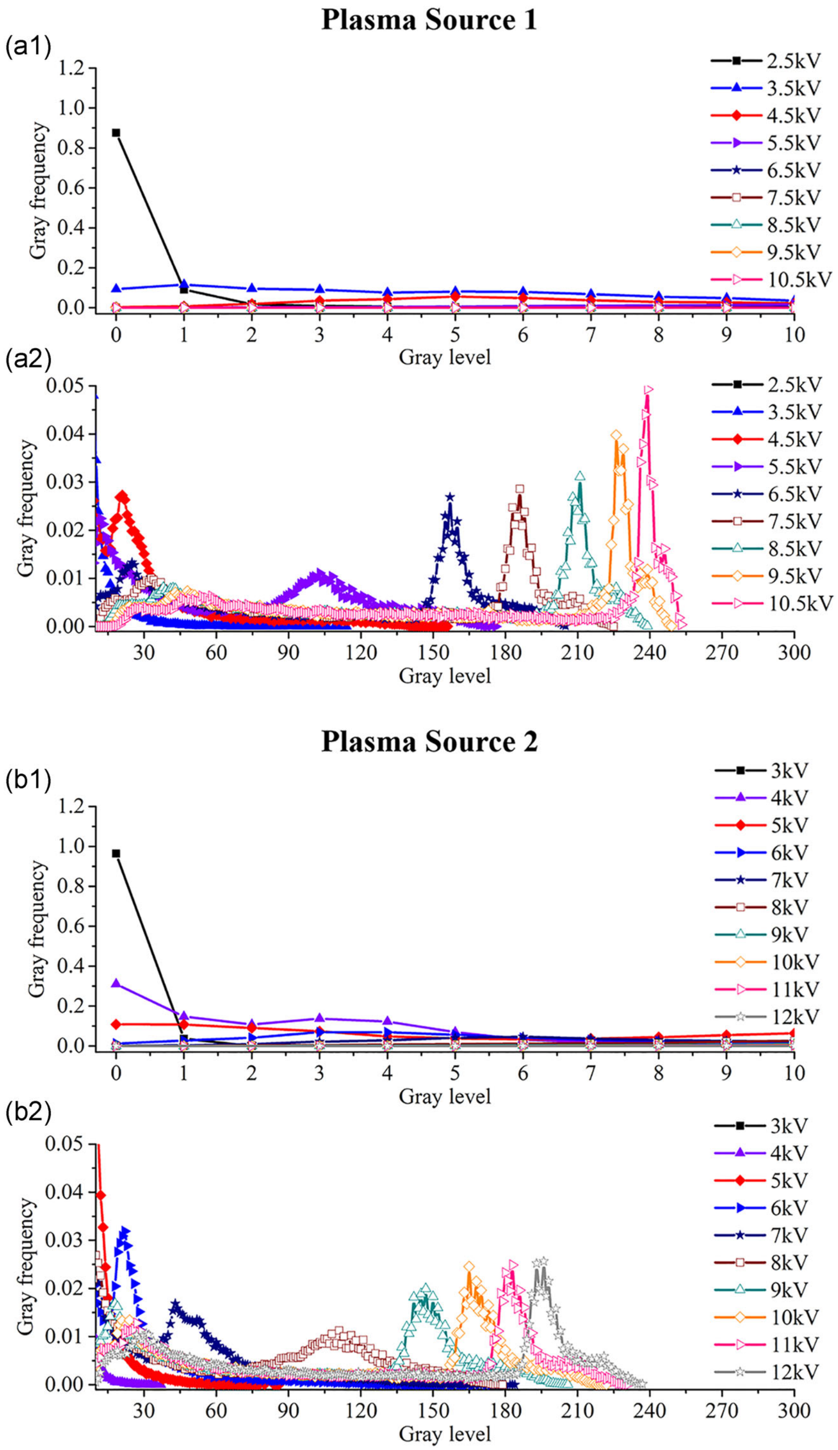

**FIGURE 6** Gray level histogram (GLH) under different $V_{\text{p–p}}$ for the two different plasma sources. (a1) GLH with a 0–10 gray level range for plasma source 1, (a2) GLH with a 10–255 gray level range for plasma source 1; (b1) GLH with a 0–10 gray level range for plasma source 2, and (b2) GLH with a 10–255 gray level range for plasma source 2

It is important to note that an obvious peak, located in the middle of the two peak clusters, is visible in the 10–255 gray level range. The purple peak ranges from the 60 to the 150 gray level in Figure 6a2 and its corresponding voltage is the voltage threshold value (the first voltage value in non-ozone mode measured under our experimental conditions) of the mode transformation detected by FTIR. The tendency of the gray frequency distribution curve of plasma sources 1 and 2 is identical. However, the peak value, the interval between the two peak clusters, and the voltage threshold value of the mode transformation differ.

## 3.4 | Feature extraction based on the GLH of the SMD

The GLH was quantitatively analyzed by extracting the features of the GLH of the SMD under different $V_{\text{p–p}}$. Figure 7 shows the extracted features of the two different

**FIGURE 7** The features extracted from the Gray level histograms in Figure 6

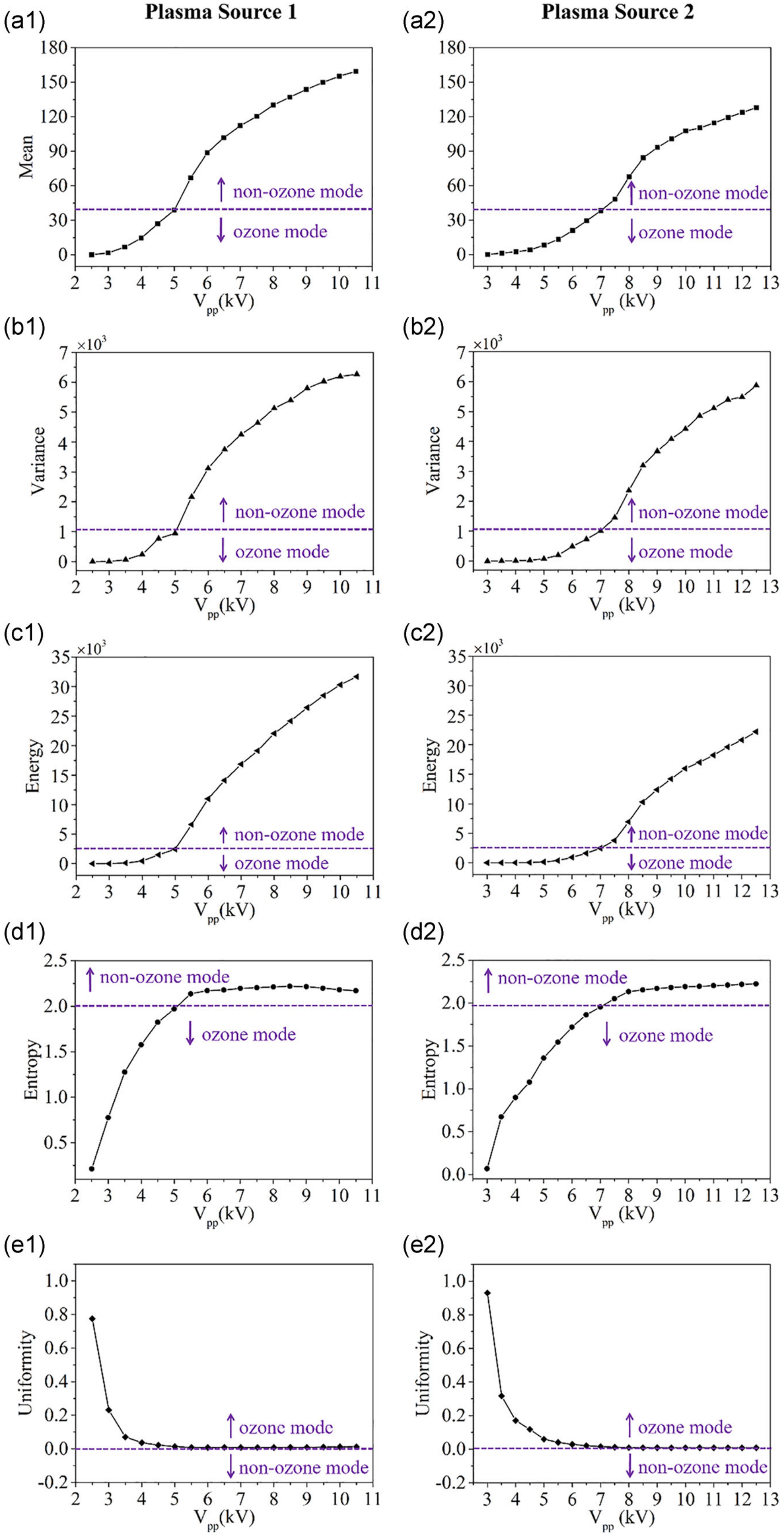

plasma sources at different $V_{p-p}$. As the $V_{p-p}$ of both plasma sources increased, the mean, variance, and energy of the GLH increased, the entropy of the GLH first increased rapidly and then remained unchanged, and the uniformity of the GLH first decreased rapidly and then remained unchanged.

Comparing the various characteristic values of the features of both plasma sources shown in Figure 7, it was found that the values at the demarcation point of the ozone and non-ozone modes were generally matched. Table 1 gives an approximate distribution range of the features extracted from the GLH to determine the operation mode. When the SMD was operated in the ozone mode, the mean was $< 40$, the variance was $< 1100$, the energy was $< 2500$, the entropy was $< 2$, and the uniformity was $> 0.012$. When the SMD was operated in the non-ozone mode, the distribution range of the corresponding features was opposite to that of the ozone mode. This was observed in both plasma sources.

## 3.5 | Visualization results of entropy and uniformity

Through feature combination and visual analysis of GLH features, entropy and uniformity were found to be used to recognize the SMD operation modes, and the visualization results are shown in Figure 8. Interestingly, when the SMD was operated in the ozone mode, the uniformity decreased rapidly as the entropy increased. When the SMD was operated in the non-ozone mode, the uniformity and entropy were clustered together. This was observed in both plasma sources. On the basis of the entropy and uniformity distribution characteristics, the division of the SMD operation modes based only on the visible image information can be realized.

## 4 | DISCUSSION

From the perspective of practical engineering applications, the SMD operation mode was divided into the ozone and non-ozone modes in this study. When the main gas phase product was $O_3$, the SMD was defined as operating in the ozone mode. Once NO, $NO_2$, HONO, or $HNO_3$ were detected in the gas phase product, the SMD was defined as operating in the non-ozone mode.

The operation mode transformation of SMD is reported to be mainly determined by the discharge power density.[23,43,44] When the discharge power density is low, the SMD operates in the ozone mode, and when the power density increases to a certain level, the SMD operates in the non-ozone mode. As shown in Figure 5, the discharge intensity, discharge brightness, and discharge area of the discharge images of SMD increase with an increase in the $V_{p-p}$. Additionally, the discharge power density of the SMD increases with an increase in the $V_{p-p}$.[42] Figure 6 shows that the features extracted from the GLH are related to the $V_{p-p}$, which is equivalently related to the discharge power density; therefore, the operation mode transformation is related to the features. It may be possible to detect the operation mode of the SMD using the features extracted from the GLH.

**TABLE 1** An approximate distribution range of the features extracted from the Gray level histogram (GLH) to determine the operation mode of surface microdischarge

| | GLH features | | | | |
|---|---|---|---|---|---|
| **Operation mode** | **Mean** | **Variance** | **Energy** | **Entropy** | **Uniformity** |
| Ozone mode | <40 | <1100 | <2500 | <2 | >0.012 |
| Non-ozone mode | >40 | >1100 | >2500 | >2 | <0.012 |

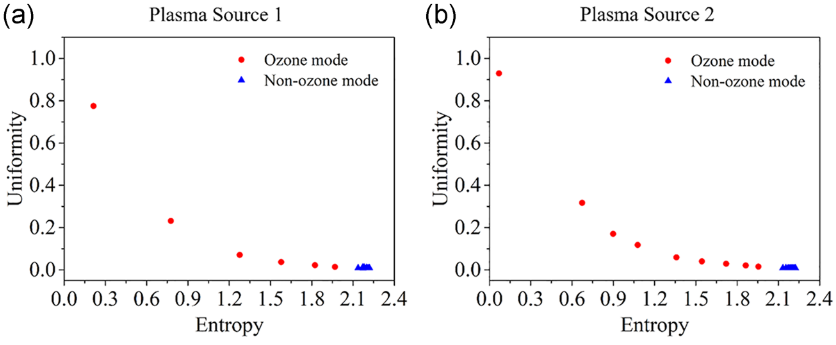

**FIGURE 8** Visualization results of entropy and uniformity corresponding to Figure 7

Digital image processing technology has been used in atmospheric pressure low-temperature plasma diagnosis, such as the discharge pattern recognition of DBD, the division of corona discharge stages, the prediction of corona discharge power, and the calculation of product concentration. However, digital image processing technology has not yet been used for the operation mode recognition of SMD. This study is the first to effectively recognize the ozone and non-ozone modes by using the GLH and the related visible-light digital image features of the SMD.

In our previous study, it was found that the dielectric properties could significantly affect the mode transformation of SMD; for example, the thickness of the dielectric sheet has a negative correlation with the mode transformation voltage.[42] Therefore, in this investigation, two different SMD plasma sources with different dielectric sheet thicknesses were used to verify the results and the effectiveness of the proposed method for mode transformation recognition through visible images of the discharge. Figure 4 shows that the breakdown voltage and transfer voltage for the different operation modes of the two SMD plasma sources are different. When the $V_{\mathrm{p-p}}$ value of the SMD plasma source 1 is 5.5 kV, the SMD enters the non-ozone mode, whereas this only occurs at a $V_{\mathrm{p-p}}$ value of 7.5 kV for the SMD plasma source 2. The electrical characteristics of the two SMD plasma sources are different under different operation modes, and the operation modes of the two SMD plasma sources cannot be divided by the same $\mathrm{V}_{\mathrm{p-p}}$. Therefore, an SMD operation mode recognition method based on the GLH is introduced in this paper. The operation modes can be detected directly by capturing SMD discharge images. Additionally, this method also offers an online and noncontact diagnostic method. It should be noted that the camera parameters (aperture size, exposure time, ISO size, and others) were the same for the image capturing process of the two different SMD plasma sources. The results indicate that the SMD operation modes can be effectively identified by this method and demonstrate that this method has a certain universality.

Our previous study investigated the relationship between the proportion of the RGB chromaticity components of the SMD discharge images and their operation modes.[41] The study found that the RGB chromaticity components were also related to the mode transformation. When the $V_{\mathrm{p-p}}$ for the same SMD device with plasma source 1 used in this study increased from 2.5 to 5 kV in the ozone mode, the Δ(B–G)% sharply increased and reached a maximum value (46.94%) at 5 kV. Then, the Δ(B–G)% decreased with a further increase in the $V_{\mathrm{p-p}}$. This demarcation point is consistent with the mode transition point measured by FTIR (at 5 kV). However, because the curve is parabolic, it still required the electrical parameter to identify the operation modes by combining the Δ(B–G)% and the $V_{\mathrm{p-p}}$. In this study, we used the GLH method to further optimize the online operation mode recognition of the SMD based on visible images. The GLH feature values and the range of the ozone and non-ozone modes were divided, and a new method is proposed to recognize the operation mode of SMD based only on the GLH features.

The proposed method does not depend on the relevant electrical parameters but is only related to the visible light emitted by the SMD. Only the optical information in the visible light digital images of the SMD needs to be extracted, effectively avoiding the influence of measurement errors and electromagnetic interference. Compared with the traditional recognition method, this method is simple and reliable, the detection cost is low, and there is no need for complicated detection devices and detection steps.

## 5 | CONCLUSIONS

This study investigated the visible information of SMD under different modes and proposed an operation mode recognition method based on the GLH features. The gray frequency distribution curve gradually extended its distribution range as the $V_{\mathrm{p-p}}$ was increased, and two peak clusters appeared in the 10–255 gray level range. The values of the mean, variance, energy, entropy, and uniformity features of the GLH at the mode transformation point were approximately the same for both SMD plasma sources. The visualization map of the entropy and uniformity shows the distribution characteristics of the ozone and non-ozone modes and can offer fast, noncontact, and low-cost online monitoring for the operation mode recognition of SMD. In the future, the intrinsic relationship between the features of GLH and the SMD discharge needs to be further studied.

## DATA AVAILABILITY STATEMENT

The data that support the findings of this study are available from the corresponding author upon reasonable request.

## ORCID

*Zilan Xiong* http://orcid.org/0000-0003-1095-3959

## REFERENCES

[1] L. Hansen, B. M. Goldberg, D. Feng, R. B. Miles, H. Kersten, S. Reuter, *Plasma Sources Sci. Technol.* **2021**, *30*, 045004.

[2] A. Bisag, P. Isabelli, R. Laurita, C. Bucci, F. Capelli, G. Dirani, M. Gherardi, G. Laghi, A. Paglianti, V. Sambri, V. Colombo, *Plasma Processes Polym.* **2020**, *17*, e2000154.

[3] D. Breden, K. Miki, L. L. Raja, *Plasma Sources Sci. Technol.* **2012**, *21*, 034011.

[4] Z. Wang, C. Feng, L. Gao, C. Liu, H. Ding, *J. Phys. D: Appl. Phys.* **2021**, *54*, 145201.

[5] S. Hofmann, A. F. H. van Gessel, T. Verreycken, P. Bruggeman, *Plasma Sources Sci. Technol.* **2011**, *20*, 065010.

[6] J. M. Williamson, D. D. Trump, P. Bletzinger, B. N. Ganguly, *J. Phys. D: Appl. Phys.* **2006**, *39*, 4400.

[7] P. Luan, L. J. Bastarrachea, A. R. Gilbert, R. Tikekar, G. S. Oehrlein, *Plasma Processes Polym.* **2019**, *16*, e1800193.

[8] C. Y. T. Tschang, M. Thoma, *J. Phys. D: Appl. Phys.* **2020**, *53*, 055201.

[9] T. Shimizu, J. L. Zimmermann, G. E. Morfill, *New J. Phys.* **2011**, *13*, 023026.

[10] D. Li, D. Liu, T. He, Q. Li, X. Wang, M. G. Kong, *Phys. Plasmas* **2015**, *22*, 123501.

[11] G. S. Dijksteel, M. M. W. Ulrich, M. Vlig, A. Sobota, E. Middelkoop, B. K. H. L. Boekema, *Ann. Clin. Microbiol. Antimicrob.* **2020**, *19*, 37.

[12] S. Bekeschus, P. Favia, E. Robert, T. von Woedtke, *Plasma Processes Polym.* **2019**, *16*, e1800033.

[13] E. A. J. Bartis, P. Luan, A. J. Knoll, D. B. Graves, J. Seog, G. S. Oehrlein, *Eur. Phys. J., D* **2016**, *70*, 25.

[14] A. J. Knoll, P. Luan, A. Pranda, R. L. Bruce, G. S. Oehrlein, *Plasma Processes Polym.* **2018**, *15*, e1700217.

[15] D. Cui, Y. Yin, J. Wang, Z. Wang, H. Ding, R. Ma, Z. Jiao, *Front. Plant Sci.* **2019**, *10*, 1322.

[16] J.-S. Song, M. J. Lee, J. E. Ra, K. S. Lee, S. Eom, H. M. Ham, H. Y. Kim, S. B. Kim, J. Lim, *J. Phys. D: Appl. Phys.* **2020**, *53*, 314002.

[17] E. Moreau, *J. Phys. D: Appl. Phys.* **2007**, *40*, 605.

[18] T. C. Corke, C. L. Enloe, S. P. Wilkinson, *Annu. Rev. Fluid Mech.* **2010**, *42*, 505.

[19] R. Zhou, R. Zhou, A. Mai-Prochnow, X. Zhang, Y. Xian, P. J. Cullen, K. Ostrikov, *J. Phys. D: Appl. Phys.* **2020**, *53*, 174003.

[20] Y. Song, D. Liu, Q. Lu, Y. Xia, R. Zhou, D. Yang, L. Ji, W. Wang, *IEEE Trans. Plasma Sci.* **2015**, *43*, 821.

[21] X. Pei, D. Gidon, Y.-J. Yang, Z. Xiong, D. B. Graves, *Chem. Eng. J.* **2019**, *362*, 217.

[22] P. Olszewski, J. Li, D. Liu, J. L. Walsh, *J. Hazard. Mater.* **2014**, *279*, 60.

[23] M. J. Pavlovich, D. S. Clark, D. B. Graves, *Plasma Sources Sci. Technol.* **2014**, *23*, 065036.

[24] T. Shimizu, Y. Sakiyama, D. B. Graves, J. L. Zimmermann, G. E. Morfill, *New J. Phys.* **2012**, *14*, 103028.

[25] Y. Sakiyama, D. B. Graves, H.-W. Chang, T. Shimizu, G. E. Morfill, *J. Phys. D: Appl. Phys.* **2012**, *45*, 425201.

[26] T. Maisch, T. Shimizu, G. Isbary, J. Heinlin, S. Karrer, T. G. Klämpfl, Y.-F. Li, G. E. Morfill, J. L. Zimmermann, *Appl. Environ. Microbiol.* **2012**, *78*, 4242.

[27] W. Xi, W. Wang, Z. Liu, Z. Wang, L. Guo, X. Wang, M. Rong, D. Liu, *Plasma Sources Sci. Technol.* **2020**, *29*, 095013.

[28] E. Simoncelli, J. Schulpen, F. Barletta, R. Laurita, V. Colombo, A. Nikiforov, M. Gherardi, *Plasma Sources Sci. Technol.* **2019**, *28*, 095015.

[29] C. Lu, J. Dai, N. Dong, Y. Zhu, Z. Xiong, *Plasma Processes Polym.* **2020**, *17*, e2000100.

[30] F. Capelli, S. Tappi, T. Gritti, A. C. de Aguiar Saldanha Pinheiro, R. Laurita, U. Tylewicz, F. Spataro, G. Braschi, R. Lanciotti, F. Gómez Galindo, V. Siracusa, S. Romani, M. Gherardi, V. Colombo, V. Sambri, P. Rocculi, *Appl. Sci.* **2021**, *11*, 4177.

[31] B. Li, Y. Yu, M. Ye, *Express* **2019**, *1*, 015017.

[32] Z. Xiong, D. B. Graves, *J. Phys. D: Appl. Phys.* **2017**, *50*, 05LT01. https://doi.org/10.1088/1361-6463/50/5/05LT01

[33] Z. Xiong, R. Huang, Y. Zhu, K. Luo, M. Li, Z. Zou, R. Han, *Plasma Processes Polym.* **2021**, *18*, e2000204.

[34] Z. Wang, C. Feng, L. Gao, H. Ding, *Phys. Plasmas* **2018**, *25*, 063523.

[35] A. A. Abdelaziz, T. Ishijima, T. Seto, N. Osawa, H. Wedaa, Y. Otani, *Plasma Sources Sci. Technol.* **2016**, *25*, 035012.

[36] T. Maisch, T. Shimizu, G. Isbary, J. Heinlin, S. Karrer, T. G. Klämpfl, Y. Li, G. Morfill, J. L. Zimmermann, *Appl. Environ. Microb.* **2012**, *78*, 4242.

[37] Y. Wu, Q. Ye, X. Li, D. Tan, *IEEE Trans. Plasma Sci.* **2012**, *40*, 1371.

[38] Z. Guo, Q. Ye, F. Li, Y. Wang, *IEEE Trans. Dielectr. Electr. Insul.* **2019**, *26*, 1448.

[39] Z. Zou, R. Han, C. Lu, Z. Xiong, *Plasma Processes Polym.* **2021**, *18*, e2000139.

[40] D. S. Prasad, B. S. Reddy, *IEEE Trans. Dielectr. Electr. Insul.* **2017**, *24*, 75.

[41] W. Du, C. Lu, Z. Xiong, Z. Tang, C. Zhao, X. Chen, in *IEEE 4th Int. Electr. Energy Conf.* (CIEEC), Wuhan, China **2021**. https://doi.org/10.1109/CIEEC50170.2021.9511033

[42] C. Lu, X. Chen, Y. Wang, Y. Zhu, Z. Zou, Z. Xiong, *Plasma Processes Polym.* **2021**, *121*, 800. https://doi.org/10.1002/ppap.202100107

[43] M. J. Pavlovich, H.-W. Chang, Y. Sakiyama, D. S. Clark, D. B. Graves, *J. Phys. D: Appl. Phys.* **2013**, *46*, 145202.

[44] M. J. Pavlovich, Y. Sakiyama, D. S. Clark, D. B. Graves, *Plasma Processes Polym.* **2013**, *10*, 1051.

**How to cite this article:** C. Lu, Z. Xiong, *Plasma Processes Polym.* **2022**, e2100205. https://doi.org/10.1002/ppap.202100205